Journal of Energy Storage 34 (2021) 102176

Contents lists available at ScienceDirect

Journal of Energy Storage

journal homepage: www.elsevier.com/locate/est

$Sr(NH_3)_8Cl_2$-Expanded Natural Graphite composite for thermochemical heat storage applications studied by *in-situ* neutron imaging

Perizat Berdiyeva [a], Anastasiia Karabanova [b], Didier Blanchard [b], Bjørn C. Hauback [a], Stefano Deledda [a,*]

[a] Department for Neutron Materials Characterization, Institute for Energy Technology, P.O. Box 40, Kjeller NO-2027, Norway
[b] Department of Energy Conversion and Storage, Technical University of Denmark, Fysikvej, Lyngby DK-2800, Denmark

ARTICLE INFO

Keywords:
Metal halide composites
Thermochemical heat storage
Ammonia sorption
Neutron imaging

ABSTRACT

This work presents an *in-situ* neutron imaging study of the ammonia sorption reaction in a $SrCl_2$-Expanded Natural Graphite (ENG) composite loaded into a honeycomb-shaped stainless-steel scaffold and enclosed in a thermochemical heat storage (THS) reactor prototype. The performance of $SrCl_2/Sr(NH_3)_8Cl_2$-ENG under different pressures and temperatures was investigated and the spatio-temporal content of ammonia was calculated from neutron radiograms. Quantitative image analysis revealed the formation of $Sr(NH_3)_8Cl_2$ upon ammonia uptake, while the desorption studies revealed a partial ammonia desorption resulting in the formation of the monoamine phase $Sr(NH_3)Cl_2$ via a stepwise release of ammonia. Neutron imaging also allowed the indirect evaluation of the stainless-steel honeycomb heat conductivity and showed that heat is transferred prevalently via the ENG matrix. Finally, neutron tomography of the reactor prototype was performed to ensure the stability of the THS system and composite material throughout the ammonia cycling experiments.

1. Introduction

Thermal energy storage and reutilization of the waste heat can give a significant contribution to reduce our carbon footprint. Different types of thermally driven materials and systems for both large and small scale applications have been developed in the past decade [1–4]. Among the various types of the thermal energy storage technologies, thermochemical heat storage (THS) systems have gained high interest and are considered as promising systems [5–7]. They can be operated using hydrates or ammines forming carbonates or metal halides for high, low or medium temperature storage, respectively. The salt-ammonia working pairs have shown high efficiency and cyclability compared to other solutions [8]. Besides, metal halide ammines have also been studied as potential hydrogen and ammonia storage materials [9–13].

The low temperature $SrCl_2$-NH_3 working pair has been extensively investigated by various techniques to characterize its kinetics, reaction pathways and cyclability [14–17]. The chemical reaction between $SrCl_2$ and NH_3 proceeds with the formation of $Sr(NH_3)_8Cl_2$ octammine at room temperature (RT) with a volume expansion of the material by up to 300 %. In the desorption process, NH_3 release generally results in the formation of $Sr(NH_3)Cl_2$ monoammine [14] at 40-50 °C under 1 bar of NH_3. Alternatively, the formation of $Sr(NH_3)_2Cl_2$ diammine can precede the formation of monoammine under selected NH_3 pressures [15]. The full NH_3 desorption occurs above 150 °C against 1 bar of NH_3. The desorption reaction results in a contraction of the material volume and formation of macro and microporous structures within the grains [18]. The extreme volume increase is the main drawback of most salt-ammonia based working pairs. If no precautions are applied, this behavior can limit their applications on account of system safety and drastically reduce the heat transfer because of the formed porous structure. Several studies have shown the possibility to circumvent the volume expansion problem in various salt-ammonia working pairs by mixing the salts with expanded natural graphite (ENG) and thus forming composites [19–23]. In addition, thermal studies showed up to 182 % increase in the thermal conductivity for $SrCl_2$-ENG composites when compared to the pure salt [19,24,25. While the ENG shows no affinity to NH_3 [26], it can help to control the volume expansion in $Sr(NH_3)_8Cl_2$, by acting as a buffer.

The work presented here shows an *in-situ* neutron imaging study on a $SrCl_2$-ENG composite placed in a stainless-steel honeycomb heat exchanger mounted inside a model THS reactor. The honeycomb heat exchanger represents the basic unit of a THS reactor prototype. The full-

* Corresponding author.
E-mail address: stefano.deledda@ife.no (S. Deledda).

https://doi.org/10.1016/j.est.2020.102176
Received 15 September 2020; Received in revised form 14 November 2020; Accepted 5 December 2020
Available online 25 December 2020

size THS reactor will comprise eleven of these honeycomb discs with a total volume of 0.5 L. Neutron imaging offers the unique possibility to analyze the spatio-temporal ammonia content in the composite material due to the high penetration power and the strong interaction of neutrons with hydrogen [27]. Neutron imaging, as a complimentary technique to X-ray imaging [28], provides a valuable information about inner structures of bulk materials. The sensitivity of neutrons to hydrogen and other light elements (e.g. lithium) makes neutron imaging a powerful characterization method widely used for energy storage materials studies such as batteries, hydrogen storage systems and fuel cells [29–36].

Recently, similar neutron imaging experiments were conducted on the $SrCl_2/Sr(NH_3)_8Cl_2$ system within the same THS reactor prototype, and the fragility of the powder bed subjected to a large volume expansion was reported [37]. Furthermore, the deformation of the stainless-steel honeycomb due to the thermal expansion and mechanical stresses caused by the volume expansion during $Sr(NH_3)_8Cl_2$ formation was presented. On the contrary, our study reports a remarkable mechanical stability of $SrCl_2$-ENG during NH_3 uptake and release with only slight expansion and contraction of the composite material, providing a homogeneous NH_3 uptake and showing excellent thermal conductivity. The hydrogen present in the ammonia molecule allows to detect the areas within the honeycomb, where $Sr(NH_3)_8Cl_2$ is formed, and here it is demonstrated for the first time how the NH_3 content in composite materials within a THS reactor can be calculated from neutron radiography images. Additionally, the heat released during NH_3 absorption reaction was monitored and the efficiency of the stainless-steel honeycomb serving as a heat exchanger and sample holder within the THS reactor is discussed. Complementary neutron tomography study revealed in-depth information about the honeycomb and the THS reactor, and the obtained results are compared to the previous neutron imaging study [37]. The neutron radiography data presented here will be compared to numerical simulations using COMSOL Multiphysics modeling software. It is integrated with calculation of thermal and mass flow within the reactor including thermochemistry of the materials with a high degree of accuracy. The ammonia cycling and the subsequent heat transfer studies provided by numerical modeling will help to optimize the THS reactor design and obtain high heat power [38].

2. Experimental

2.1. Sample preparation

The $SrCl_2$-ENG composite was prepared by impregnation of expanded natural graphite (ENG) sheets (from SGL Carbon, 95 % purity) with $SrCl_2$ (from AMMINEX, 99.9 % purity) by submerging the ENG into $SrCl_2{\cdot}H_2O$ for 72 hours. Prior to the impregnation process, ENG was dried at 180 °C for 8 hours and then soaked into ethanol for 2 hours for reducing the surface tension between non-polar ENG and polar $SrCl_2{\cdot}H_2O$ [39]. The impregnated ENG was then dried in an oven at 90 °C for 12 hours and further dehydrated in vacuum at 300 °C for 12 hours. Using this impregnation method, a $SrCl_2$-ENG composite with 76 wt% of $SrCl_2$ and 24 wt% of ENG was obtained. The composite sheets were obtained by compressing the $SrCl_2$-ENG composites, resulting in a packed density of 543 $kg{\cdot}m^{-3}$. Hexagonal pellets with height of 10 mm were cut out from the $SrCl_2$-ENG composite sheets and loaded into the stainless-steel honeycomb half disc (See Fig. S1).

2.2. THS set-up

The $SrCl_2$-ENG composite pellets (total mass of 8.4 g) were loaded into a stainless-steel honeycomb half-disc containing a heating element with thermocouple (T_h) and a second thermocouple (T_s) to monitor the sample temperature during ammonia cycling. T_s was inserted to the top of the honeycomb and surrounded by stainless-steel walls with thickness of ~2.5 mm. The honeycomb half-disc was then inserted into the THS reactor, which was connected to an absorption/desorption rig (see Fig. 1). The detailed parameters of the THS reactor are described elsewhere [37]. Prior to the neutron imaging experiment the sample was dried at 200 °C under dynamic vacuum for 3 hours, to remove any possible water impurities. A reservoir with 100 g of $Sr(NH_3)_8Cl_2$ powder, denoted as the 'ammonia reservoir', served as the ammonia source and was connected to the THS reactor with stainless steel tubes. A flowmeter with a readout range of 0 – 200 $ml{\cdot}min^{-1}$ was implemented between the THS reactor and the reservoir in order to monitor the NH_3 gas flow during cycling. A magnetic valve (*M*) connected to the THS reactor ensured a remote control of the NH_3 gas flow between $SrCl_2$-ENG in the honeycomb and the reservoir. A pressure transducer (*P*) mounted between the flowmeter and the reservoir allowed a continuous monitoring of the pressure.

The ammonia absorption in $SrCl_2$-ENG was achieved by heating up $Sr(NH_3)_8Cl_2$ in the ammonia reservoir, to release NH_3 into the setup, while the ammonia desorption was studied by heating ammoniated $Sr(NH_3)_8Cl_2$-ENG in the THS reactor at various temperatures. Such closed system ensured safe handling of NH_3 gas during the experiment.

2.3. Neutron imaging set-up

The neutron imaging experiments were performed at the NeXT beamline (D50) [40] at the Institute Laue-Langevin (ILL) research reactor in Grenoble, France. A cold neutron beam with a flux of $1.5{\cdot}10^8$ $n{\cdot}cm^{-2}{\cdot}s^{-1}$ was collimated by a 23 mm pinhole (L/D ~ 435) and transmitted through the sample. The sample was mounted in front of a Gadox scintillator screen with a field of view 10 cm x 10 cm and a thickness of 50 μm. The scintillated light was captured by a CMOS camera (Hamamatsu Orca 4V2) providing images with a time resolution of 1 s. For three sequential radiography images, one average image was produced.

The radiography images were normalized and analyzed using ImageJ [41] and the transmission of the $SrCl_2/Sr(NH_3)_8Cl_2$-ENG composite material was calculated according to:

$$I = I_0 e^{-\mu x} \tag{1}$$

where I is the intensity transmitted through the sample, I_0 is the incident intensity, μ is the linear attenuation coefficient and x is the sample thickness.

The neutron transmission values of NH_3 absorbed in the composite material were obtained by dividing the overall stack of images by the first image (for absorption) or by the last image (for desorption) in order to remove the $SrCl_2$-ENG contribution from the images and to observe only absorbed or desorbed NH_3 in the radiogram. The mean transmission values for the NH_3 were obtained from selected hexagon-shaped areas within each cell of the honeycomb. The density of NH_3 was calculated according to:

$$\rho_{NH_3} = \frac{\left(\mu_{Sr(NH_3)_8Cl_2-ENG} - \mu_{SrCl_2-ENG}\right) * M}{N_A * \sigma_{NH_3}} \tag{2}$$

where $\mu_{Sr(NH3)8Cl2\text{-}ENG}$ is the attenuation coefficient of the ammoniated composite, $\mu_{SrCl2\text{-}ENG}$ is the attenuation coefficient of the composite without ammonia, M is the molar mass of ammonia, N_A is Avogadro constant and σ_{NH3} is the total neutron cross section of ammonia. The mass of ammonia m_{NH3} is calculated from the density given by Equation-2 multiplied with the volume of NH_3 obtained from each radiogram. Then the gravimetric NH_3 content (wt%) in $Sr(NH_3)_xCl_2$ during absorption and desorption was calculated from:

$$x_{NH_3} = \frac{m_{NH_3}}{m_{NH_3} + m_{SrCl_2}} * 100\% \tag{3}$$

where m_{SrCl2} is the mass of the $SrCl_2$ in the composite material in the initial state.

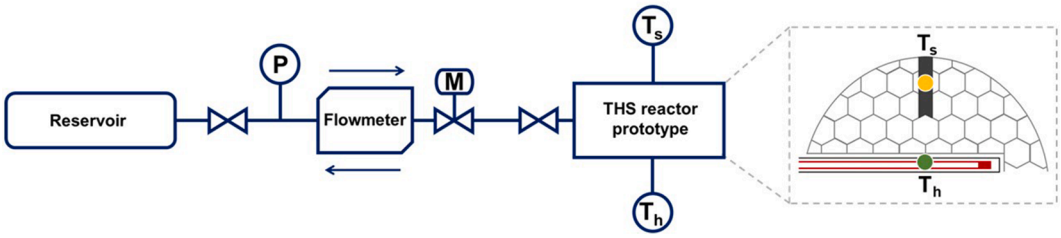

Fig. 1. Left: schematic view of the setup. P, T_h and T_s represent the points where the pressure, temperature of the heater and the sample temperature were monitored, respectively. M denotes the position of the magnetic valve. The arrows above and beneath the flowmeter show the NH_3 gas flow during the absorption and desorption, respectively. Right: Schematic of the honeycomb half-disc with marked positions of T_h and T_s. The heating element below the honeycomb is marked with red color. (For interpretation of the references to color in this figure legend, the reader is referred to the web version of this article.).

Neutron tomography of the composite material was carried out by rotating the THS reactor over a 360° range at 0.225° per step and resulting in 1600 projections (one image per step). The initial state, the absorbed and desorbed states of the composite material were scanned and reconstructed using XAct software [42] and visualized with VG Studio Max© software [43].

3. Results and discussions

3.1. Ammonia sorption and heat storage properties of the $SrCl_2$-ENG composite in the THS system

In total four NH_3 absorption desorption cycles in the $SrCl_2$-ENG composite were studied. Each absorption was followed by desorption with a dwell time to allow the THS reactor or the ammonia reservoir to cool down.

Absorption reactions were conducted at RT and at different NH_3 gas pressures. Fig. 2a depicts the evolution of the NH_3 gas pressures during the four absorption processes. The first (Absorption-1, blue curve) and second (Absorption-2, red curve) absorption were performed at similar NH_3 pressures of ~2.5 bar which increased up to 2.7 bar due to the saturation of $Sr(NH_3)_8Cl_2$-ENG while the NH_3 gas was still provided by the ammonia reservoir. The third absorption (Absorption-3, green curve) was achieved under 1.5 bar of NH_3 and the pressure remained almost constant during the whole absorption process. This is due to the slower NH_3 absorption in the $SrCl_2$ salt under lower NH_3 gas pressures, allowing for less variations in the total pressure of the system. The fourth absorption (Absorption-4, yellow curve) started at 3 bar of NH_3 and the pressure was immediately increased up to 3.5 bar over 30 min by increasing the temperature of the ammonia reservoir. The higher NH_3 gas pressure in this case resulted in fast absorption reaction with the subsequent drop in the pressure down to ~3.3 bar.

The NH_3 gas flow during Absorption-1 and -2 showed similar behavior with the flow increase up to 200 ml·min^{-1} at the very beginning of the experiment and then reduced to 0 ml·min^{-1}. The flowmeter detected the NH_3 gas flow end close to 2 hours, indicating that the Absorption-1 and -2 were complete at that time. The NH_3 flow during Absorption-3 increased to 140 ml·min^{-1} and slowly reduced by the end of the absorption reaction of 3.2 hours. Absorption-4, conducted at higher NH_3 pressure (3.5 bar), was complete in over 1 hour as the flowmeter recorded NH_3 gas flow termination. Due to the saturation of the flowmeter at its highest possible readout of 200 ml·min^{-1} during some absorption and desorption cycles (Fig. 3b), the amount of ab-/desorbed NH_3 is underestimated, and therefore the total amount of NH_3 was not calculated from flowmeter data.

Heat is released during the $Sr(NH_3)_8Cl_2$ formation due to the exothermic absorption reaction. The temperature at the top of the honeycomb (T_s) was therefore recorded in order to evaluate the temperature increase during absorption. Fig. 2c shows the temperatures measured as $Sr(NH)_8Cl_2$-ENG is formed during the absorption processes 1 to 4. At Absorption-1 and -2 (~2.5 bar of NH_3) the thermocouple registered up to ~46 °C, while at 3 bar and 1.5 bar of NH_3 the temperature reached up to 53.5 °C and 33.1 °C, respectively. These results show that the heat released during absorption processes can be controlled by the NH_3 gas pressure applied to the system.

The four NH_3 desorption processes were carried out under 0.8 bar of NH_3 and temperatures between 100 °C and 200 °C. Fig. 3a shows the NH_3 pressure increase at the start of each desorption due to the released NH_3 which was then absorbed in the ammonia reservoir resulting in a subsequent pressure drop. The first (Desorption-1, blue curve) and the last (Desorption-4, yellow curve) desorption were conducted at the same temperature (200 °C). In both cases, the pressure raised to 1.2 bar in 30 min, remained constant for a short time and then decreased and the desorption process was complete in less than 1 hour.

During the second desorption (Desorption-2, red curve) at 150 °C, the pressure increases up to 1.1 bar and reduces to 0.9 bar as the NH_3 desorption is complete in ~1.3 hours. For Desorption-3 (green curve), conducted at the lowest temperature of 100 °C, the pressure increased only up to 0.95 bar. This shows that the pressure change during the desorption processes depend on the heating temperature of the Sr $(NH_3)_8Cl_2$-ENG composite material.

The temperature of the sample, T_s, was also measured during the

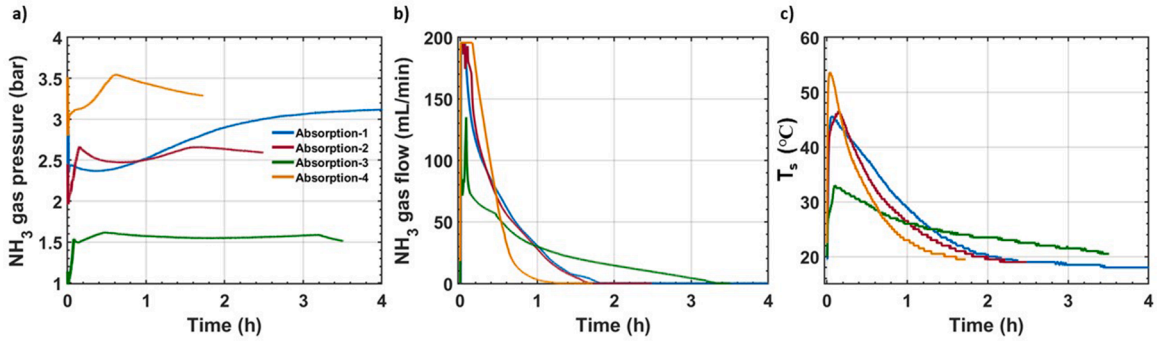

Fig. 2. The parameters measured during absorption processes: (a) NH_3 gas pressure, (b) NH_3 gas flow and (c) $Sr(NH_3)_8Cl_2$-ENG composite temperature, T_s.

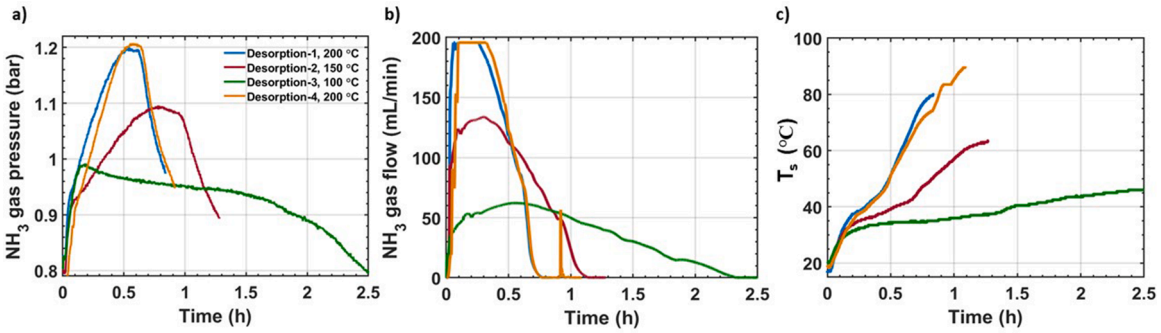

Fig. 3. The parameters measured during desorption processes: (a) NH_3 gas pressure, (b) NH_3 gas flow and (c) $Sr(NH_3)_8Cl_2$-ENG composite temperature, T_s.

desorption cycles at the top of the honeycomb to evaluate the heat distribution over the honeycomb area (Fig. 3c). The highest T_s is 83.5 °C when the sample was heated at 200 °C (Desorption-1 and -4). The slight increase up to 90°C in Desorption-4 was due to increasing the set temperature of the heating element to 230 °C at the end of the Desorption-4. At the lower desorption temperatures of 150 °C (Desorption-2) and 100 °C (Desorption-3), T_s reached only 63.5 °C and 46 °C, respectively. The difference in recorded temperature between the heating element and the thermocouple is mainly due to the distance between the heating element and the thermocouple. In addition, the heat distribution over the honeycomb area might be affected by the endothermic nature of the desorption reactions. It should be also noted that the thermocouple was positioned in between the ~2.5 mm stainless steel walls which might prevent reading the actual temperature of the sample during the sorption processes.

3.2. Neutron radiography

The four cycles of NH_3 absorption and desorption in the $SrCl_2$-ENG composite under different temperatures and NH_3 pressures were investigated by *in-situ* neutron radiography. After the last desorption the sample was heated up to 230 °C under vacuum to remove all possible NH_3 left in the composite material. Due to the attenuation of neutron beam by hydrogen present in ammonia, the NH_3 uptake by $SrCl_2$-ENG composite results in formation of dark areas in the radiograms, and during the desorption the dark areas in the radiogram become brighter as a result of the ammonia release. The NH_3 absorption reaction was homogeneous over the honeycomb area (See Fig. S2), but the desorption showed dependence of the heat transfer properties on the stainless-steel honeycomb.

Fig. 4 shows the normalized radiography images after 30 min of the four desorption performed on $Sr(NH_3)_8Cl_2$-ENG at different temperatures. The lower heating temperatures result in slower NH_3 release. The desorption of NH_3 starts from the areas of the honeycomb close to the heating element placed at its bottom, and thus showing the relatively poor heat conductivity of the stainless-steel honeycomb. In all four desorption cases, the NH_3 desorbed from each cell in the honeycomb is a result of the heat transferred through the composite material rather than the heated walls of the honeycomb cells.

For calculating the NH_3 content, several areas of the honeycomb were selected and numbered (see Fig. S3). Fig. 5a depicts a schematic view of the honeycomb with four cells marked as cell-3, -5, -7 and -12. The NH_3 contents of $Sr(NH_3)_8Cl_2$ formed in these selected cells calculated according to Eq. (3) are plotted as function of time in Fig. 5b–i. For Absorption-1 (~2.5 bar of NH_3) the total NH_3 uptake reaches up to 45.7 wt% in cell-5 (Fig. 5b) which is very close to the theoretical 46.2 wt% for a complete absorption. The NH_3 content in the cell-3, -7 and -12 reached 44.9 wt%, 45.1 and 43.5 wt%, respectively. Cell-12 shows the lowest NH_3 content throughout the cycling. This might be due to a slight inhomogeneity of the $SrCl_2$ content in the ENG matrix, which might differ

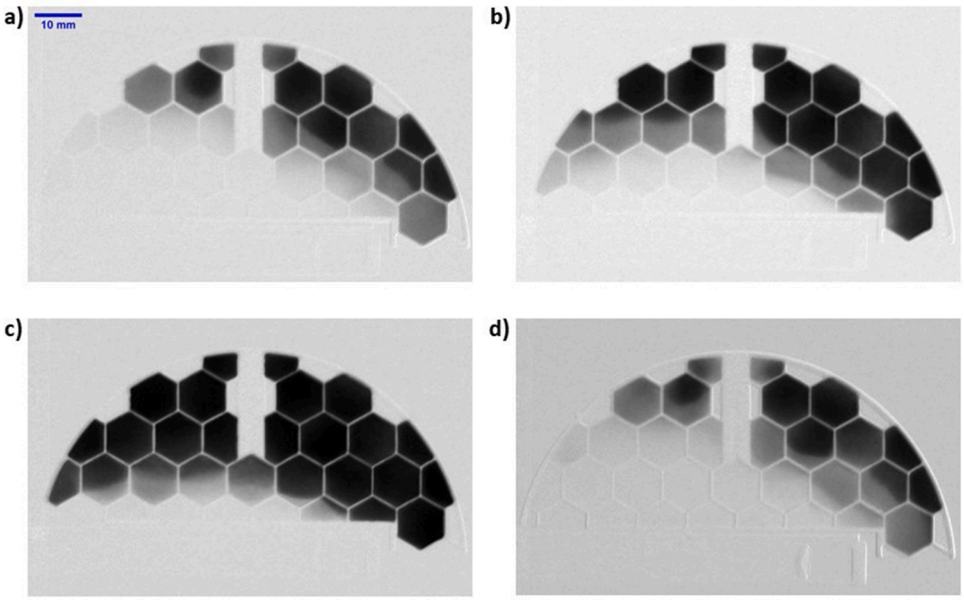

Fig.4. Series of normalized neutron radiography images after 30 min of (a) Desorption-1 at 200 °C, (b) desorption-2 at 150 °C (c) desorption-3 at 100 °C and (d) desorption-4 at 200 °C.

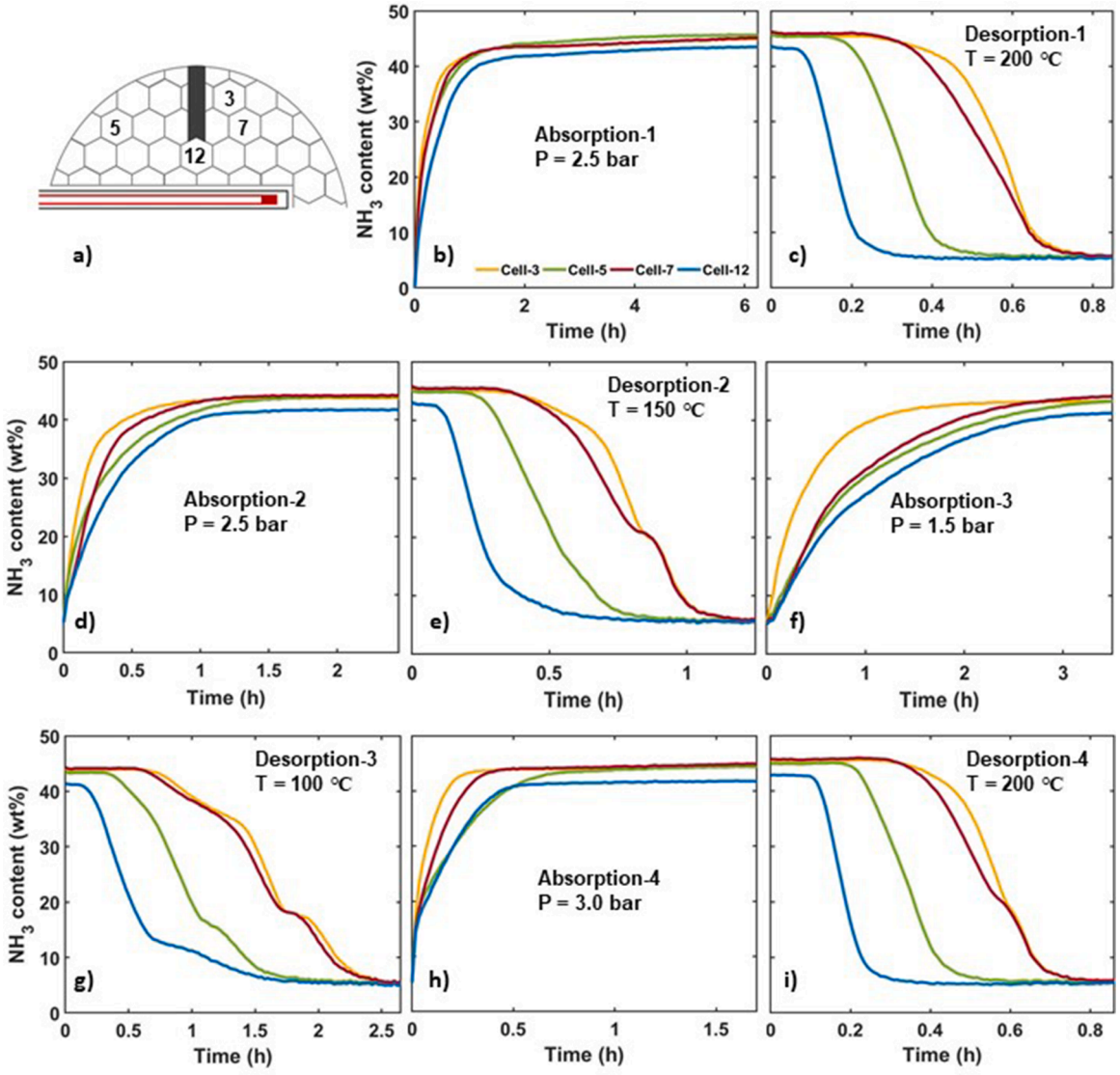

Fig. 5. (a) Schematic view of the honeycomb with the selected cells: cell 3 – yellow, cell 5 – green, cell 7 – red and cell 12 – blue. The heating element below the honeycomb is marked with red color. (b–i) NH_3 content (wt%) in the selected cells during the absorption processes at RT and different pressures P, and during the desorption processes at pressure P=0.8 bar and different temperatures T. Absorption-2, -3 and -4 start from 5.4-5.8 wt%. (For interpretation of the references to color in this figure legend, the reader is referred to the web version of this article.).

from cell to cell and deviate from the overall value of 76 wt%. Finally, the ammoniated salt $Sr(NH_3)_8Cl_2$ represented 85 wt% of the composite, 15 wt% being the ENG and the gravimetric NH_3 capacity of the Sr $(NH_3)_8Cl_2$-ENG composite evaluated to be of 38.8 wt%. The results for Desorption-1 at 200 °C (Fig. 5c) show how the relative distance of the different cells from the heating element affects the desorption time. Sr $(NH_3)_8Cl_2$ in cell-5 and -12 desorbed NH_3 in ~0.3-0.5 hours and for cell-7 and -3 in about 0.7 hours. Only 7 out of the 8 NH_3 moles were released and the monoamine was obtained with the NH_3 content kept as 5.4-5.7 wt%. The NH_3 wt% for monoammine was calculated relative to octammine. The change between $Sr(NH_3)Cl_2$ monoammine and Sr $(NH_3)_8Cl_2$ octammine occurred in all the following cycles.

Therefore, Absorption-2 starts from 5.4-5.7 wt% and then 38.4 wt% of NH_3 was absorbed resulting in 44.6 wt% of ammonia in the salt at 2.5 bar (Fig. 5d). After 2 hours, the absorption curves flatten out indicating saturation of the powder particles. The desorption at 150 °C (Desorption-2, Fig. 5e) shows that 7 moles of NH_3 are released within 1.5 hours and the desorption trend in each cell is the same as for the previous desorption. Absorption-3 at 1.5 bar of NH_3 resulted in a slow absorption process taking more than 3 hours due to the low NH_3 pressure (Fig. 5f). The obtained NH_3 content reached up to 44.3 wt% in the cells. The following Desorption-3 at 100 °C resulted in the desorption of 7 moles of NH_3 in 2.5 hours (Fig. 5g). The last cycle of the NH_3 sorption was performed at 3.0 bar for absorption of NH_3 reaching up to 45.6 wt% (Fig. 5h) and desorption at 200 °C (Fig. 5i).

The effect of the low heating temperature on the performance of the honeycomb during Desorption-2, -3 and -4 can be seen from plots in Fig. 5e, g and i. At 0.8 hours of Desorption-2 (T = 150 °C), temporary slowdowns of the desorption for cells-3 and -7 were observed as "bumps" in the curves (Fig. 5e). The desorption curves for cell-3, -5 and -7 (Fig. 5g) contain two distinct "bumps", and during Desorption-4 (T = 200 °C) the single "bump" in cell-3 and -7 appear at 0.55 hours. This is probably due to the endothermic nature of the desorption reaction and the heat dissipation within the honeycomb. It results in delayed heat transfer to the next cells and therefore slows down the ammonia release in the cells that are away from the heat source. However, the bumps in the desorption curves between 12 wt% and 20 wt% might also be the result of a multi-step desorption of NH_3. The $Sr(NH_3)_8Cl_2$ octammine releases 7 moles of NH_3 followed by $Sr(NH_3)Cl_2$ monoammine formation at 40-50 °C under 1 bar of NH_3 [14]. However, this reaction has been

reported to occur in two steps under selected NH_3 pressures and slow heating rates with the $Sr(NH_3)_2Cl_2$ diammine forming first and followed by the $Sr(NH_3)Cl_2$ monoammine [15]. The bumps observed at ~12 wt% might therefore correspond to the formation of the diamine.

A similar NH_3 uptake and release behavior was observed for the other honeycomb cells not plotted here. These data are included in the Supplementary material (See Figs. S4 and S5). The slight mismatches of the NH_3 wt% values at the end of absorption and beginning of desorption curves are likely due to at least 30 minutes waiting time for cooling down the ammonia reservoir or the THS reactor in order to proceed with the next cycling step. During that cooling time no neutron radiography measurements were performed, and some NH_3 was likely reabsorbed or further desorbed before the start of the next sorption process.

Assuming the $Sr(NH_3)_8Cl_2$ octammine formation from $SrCl_2$ during Absorption-1, only 7 moles of NH_3 were ab/desorbed during the following ab-/desorption reactions, following the reaction $Sr(NH_3)_8Cl_2 \leftrightarrow Sr(NH_3)Cl_2+7NH_3$. During the desorption processes at temperature above or equal to 150 °C and against 0.8 bar of NH_3 (Fig. 5 c, e and i) the full NH_3 desorption did not occur which is likely due to the poor heat conductivity of the stainless-steel honeycomb and loss of heat to the ambient via the THS reactor walls. Even with a heating temperature of 200 °C, the maximum temperature recorded at the honeycomb thermocouple (T_s) was 83.5 °C.

This was confirmed during our final neutron radiography experiment performed after Desoption-4 where the temperature was kept at 230 °C under dynamic vacuum for 15 min. Radiography during this final step showed a change in image intensity (See Fig. S6), indicating an additional release of NH_3 and suggesting further desorption from the remaining monoammine $Sr(NH_3)Cl_2$.

The different pressures (P) of the applied NH_3 gas during absorption processes showed that the formation of $Sr(NH_3)_8Cl_2$-ENG is faster at higher NH_3 pressures and slower at lower NH_3 pressures. Additionally, the temperature of the sample ($Sr(NH_3)_8Cl_2$-ENG) increases when the applied NH_3 gas pressure was increased (see Section 3.1) due to the exothermic absorption reaction. Therefore, the NH_3 absorption time and the heat released during absorption can be controlled by the applied NH_3 gas pressure. Meanwhile, the NH_3 desorption is governed by the heating temperature (T) of $Sr(NH_3)_8Cl_2$-ENG. At the higher temperatures the NH_3 desorption is faster whilst at the lower temperatures the NH_3 release is slower. Additionally, the lower heating temperatures during the NH_3 desorption allowed to observe the step-desorption of the NH_3 and therefore formation of $Sr(NH_3)_2Cl_2$.

3.3. Neutron tomography

Three-dimensional images of the investigated sample were reconstructed from the neutron radiograms obtained during its rotation over 360° around its axis (See Fig. S7). The information about the inner structure of the THS reactor prototype is acquired from the orthogonal planes of the 3D images, showing the arrangement of the hexagonal pellets of $SrCl_2$-ENG composite within the cells of the honeycomb. Fig. 6a shows the orthogonal view of the sample in the XY and XZ-planes before NH_3 cycling. A space between the pellets and the honeycomb walls can be seen in both planes, and thus allowing the pellets to expand and occupy the whole volume of the cells during the NH_3 absorption.

The ENG matrix in the composite acts as a buffer during NH_3 cycling limiting the expansion and contraction of $SrCl_2$-ENG during NH_3 uptake and release, respectively. Fig. 6b presents the XY and XZ-planes of the $Sr(NH_3)Cl_2$-ENG after partial NH_3 desorption. Due to the NH_3 present in the salt, the pellets still occupy a large fraction of the available volume. It can also be noticed that the expansion of the composite in the axial directions (perpendicular to the honeycomb) is not limited by the walls of the honeycomb cells. This feature of the ENG is beneficial for the heat transfer between the active material and the honeycomb, and thus allowing to increase the efficiency of the THS reactor and the system.

3.4. Comparison with the previous work

In the previous neutron imaging study of the $SrCl_2/Sr(NH_3)_8Cl_2$ system within the same THS reactor prototype only qualitative analysis of the neutron radiography data was performed [37]. Some of the $SrCl_2$ powder had fallen out of the honeycomb during the sample mounting and volume expansion resulting in continuous changes of the $SrCl_2$ powder bed thickness, which could not be determined accurately and prevented any quantitative analysis [37]. A known thickness of the investigated area is needed for quantitative analysis of neutron radiography images (see Eq. (1)). This was achieved in the present work by the confinement of $SrCl_2$ in the porous ENG matrix ensuring the stability of the $SrCl_2$-ENG composite against external forces while allowing free expansion of the powder within the porous media. The composite material provided fast absorption and desorption processes compared to the previous study proving the improvement for the reaction kinetics when the salt is confined in porous ENG matrix. The desorption of 7 moles of NH_3 from $Sr(NH_3)_8Cl_2$ powder was complete within 4 hours at 100 °C in previous results [37], while it was completed within 2.5 hours in $Sr(NH_3)_8Cl_2$-ENG composite at the similar conditions. The enhanced thermal conductivity and permeability of the $SrCl_2$-ENG composite material due to the increased porosity and thermal conductivity of ENG allowed for better heat and mass transfer during NH_3 cycling [24]. A thermal equilibrium of the system depends on the heat transfer, therefore high heating rates are required for the material with poor heat transfer (e.g. $Sr(NH_3)_8Cl_2$ powder). The high heating rate also causes the chemical non-equilibrium and the possible absence of the intermediate reaction process [26]. Meanwhile, the higher heat transfer provided by ENG allows for the thermal equilibrium at slower heating rates. This in turn helped to observe the formation of $Sr(NH_3)_2Cl_2$ diammine during NH_3 desorption at lower T=100-150 °C, which was not observed when pure $SrCl_2$ powder was used in previous studies [37]. Ultimately, an enhanced thermal conductivity is expected to improve the thermal energy storage performance of the system.

Additionally, investigation of the heat transfer efficiency of the honeycomb and the spatio-temporal NH_3 concentration in the composite material during cycling in this study provides a valuable information about the efficient performance of the THS reactor. The presented

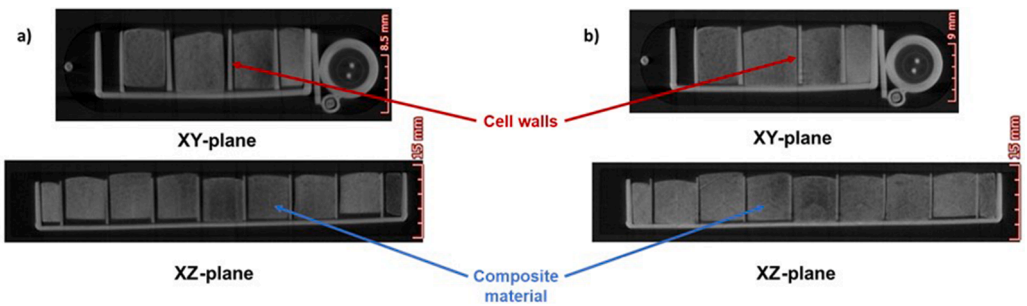

Fig. 6. The XY (top row) and XZ-plane (bottom row) views of the (a) initial $SrCl_2$-ENG composite and (b) $Sr(NH_3)Cl_2$-ENG after cycling.

neutron radiography results in this work will be compared with the numerical simulations from COMSOL Multiphysics modeling software. This modeling includes the NH_3 flow and heat transfer function of the honeycomb heat reactor which will provide high accuracy and close equivalence to the sorption reaction observed with neutron radiography.

Neutron tomography of the THS reactor prototype with $SrCl_2$/Sr$(NH_3)_8Cl_2$ system revealed the distortion of the honeycomb after NH_3 cycling, where the honeycomb back plate was bended due to the volume expansion of the sample [37]. In this work we note that the mechanical stresses on the honeycomb were minimized by confining the $SrCl_2$ in ENG matrix. Therefore, the mechanical stability of the stainless-steel honeycomb together with the limited expansion/contraction of the $SrCl_2$-ENG composite make the investigated THS reactor a safe system for the future applications.

4. Conclusion

It is demonstrated that neutron imaging is a useful technique for determination of spatio-temporal NH_3 content in Sr$(NH_3)_8Cl_2$-ENG composite pellets produced for thermochemical heat storage applications. ENG mixed with $SrCl_2$ showed excellent kinetics during the NH_3 absorption and desorption. The results from neutron radiography and tomography confirmed the mechanical stability of the $SrCl_2$-ENG composite upon cycling. The stainless-steel honeycomb in which the pellets were embedded, showed a poor heat transfer efficiency during the desorption processes resulting in an inhomogeneous NH_3 desorption process. The heat release during exothermic Sr$(NH_3)_8Cl_2$-ENG formation with the temperatures of up to $T = 53.5$ °C has been detected. The exothermic and endothermic NH_3 cycling monitored during *in-situ* neutron radiography revealed a high potential of the $SrCl_2$-ENG composite materials for the low temperature thermochemical heat storage applications.

CRediT authorship contribution statement

Perizat Berdiyeva: Methodology, Formal analysis, Investigation, Data curation, Writing - original draft, Visualization. **Anastasiia Karabanova:** Methodology, Formal analysis, Investigation, Writing - review & editing. **Didier Blanchard:** Conceptualization, Methodology, Investigation, Resources, Project administration, Writing - review & editing, Funding acquisition. **Bjørn C. Hauback:** Writing - review & editing, Supervision. **Stefano Deledda:** Conceptualization, Methodology, Investigation, Resources, Writing - review & editing, Supervision, Funding acquisition.

Declaration of Competing Interest

The authors declare that they have no known competing financial interests or personal relationships that could have appeared to influence the work reported in this paper.

Acknowledgment

This work is financially supported by NordForsk Nordic Neutron Science Programme via the Neutrons for Heat Storage (NHS) project (No. 82206). The authors thank the ILL for the allocation of neutron radiation beam time via the experiments UGA-83 (DOI: 10.5291/ILL-DATA.UGA-83) and DIR-196 (DOI: 10.5291/ILL-DATA.DIR-196) and particularly Lukas Helfen and Alessandro Tengattini for experimental assistance. Additionally, the Danish Research Council is gratefully acknowledged for the financial support via Danscatt.

Supplementary materials

Supplementary material associated with this article can be found, in the online version, at doi:10.1016/j.est.2020.102176.

References

[1] R. Parameshwaran, S. Kalaiselvam, S. Harikrishnan, A. Elayaperumal, Sustainable thermal energy storage technologies for buildings: a review, Renew. Sustain. Energy Rev. 16 (2012) 2394–2433, https://doi.org/10.1016/j.rser.2012.01.058.
[2] A. Sharma, V.V. Tyagi, C.R. Chen, D. Buddhi, Review on thermal energy storage with phase change materials and applications, Renew. Sustain. Energy Rev. 13 (2009) 318–345, https://doi.org/10.1016/j.rser.2007.10.005.
[3] T.D. Humphries, K.T. Møller, W.D.A. Rickard, M. Veronica Sofianos, S. Liu, C. E. Buckley, M. Paskevicius, Dolomite: a low cost thermochemical energy storage material, J. Mater. Chem. A 7 (2019) 1206–1215, https://doi.org/10.1039/C8TA07254J.
[4] K.T. Møller, D. Sheppard, D.B. Ravnsbæk, C.E. Buckley, E. Akiba, H.-W. Li, T. R. Jensen, Complex metal hydrides for hydrogen, Therm. Electrochem. Energy Storage Energies 10 (2017) 1645, https://doi.org/10.3390/en10101645.
[5] D.N. Harries, M. Paskevicius, D.A. Sheppard, T.E.C. Price, C.E. Buckley, Concentrating solar thermal heat storage using metal hydrides, Proc. IEEE 100 (2012) 539–549, https://doi.org/10.1109/JPROC.2011.2158509.
[6] P. Pardo, A. Deydier, Z. Anxionnaz-Minvielle, S. Rougé, M. Cabassud, P. Cognet, A review on high temperature thermochemical heat energy storage, Renew. Sustain. Energy Rev. 32 (2014) 591–610, https://doi.org/10.1016/j.rser.2013.12.014.
[7] Y. Zhang, R. Wang, Sorption thermal energy storage: concept, process, applications and perspectives, Energy Storage Mater. 27 (2020) 352–369, https://doi.org/10.1016/j.ensm.2020.02.024.
[8] T. Yan, Z.H. Kuai, S.F. Wu, Experimental investigation on a $MnCl_2$–$SrCl_2$/NH_3 thermochemical resorption heat storage system, ScienceDirect 147 (2020) 874–883, https://doi.org/10.1016/j.renene.2019.09.033.
[9] R.Z. Sørensen, J.S. Hummelshøj, A. Klerke, J.B. Reves, T. Vegge, J.K. Nørskov, C. H. Christensen, Indirect, reversible high-density hydrogen storage in compact metal ammine salts, J. Am. Chem. Soc. 130 (2008) 8660–8668, https://doi.org/10.1021/ja076762c.
[10] A. Bialy, P.B. Jensen, D. Blanchard, T. Vegge, U.J. Quaade, Solid solution barium–strontium chlorides with tunable ammonia desorption properties and superior storage capacity, J. Solid State Chem. 221 (2015) 32–36, https://doi.org/10.1016/j.jssc.2014.09.014.
[11] A. Tekin, J.S. Hummelshøj, H.S. Jacobsen, D. Sveinbjörnsson, D. Blanchard, J. K. Nørskov, T. Vegge, Ammonia dynamics in magnesium ammine from DFT and neutron scattering, Energy Environ. Sci. 3 (2010) 448–456, https://doi.org/10.1039/B921442A.
[12] T. Vegge, R.Z. Sørensen, A. Klerke, J.S. Hummelshøj, T. Johannessen, J.K. Nørskov, C.H. Christensen, 19 - Indirect hydrogen storage in metal ammines, in: G. Walker (Ed.), Solid-State Hydrogen Storage, Woodhead Publishing, 2008, pp. 533–564, https://doi.org/10.1533/9781845694944.4.533.
[13] P. Berdiyeva, A. Karabanova, J.B. Grinderslev, R.E. Johnsen, D. Blanchard, B. C. Hauback, S. Deledda, Synthesis, structure and NH_3 sorption properties of mixed $Mg_{1-x}Mn_x(NH_3)_6Cl_2$ ammines, Energies 13 (2020) 2746, https://doi.org/10.3390/en13112746.
[14] R.E. Johnsen, P.B. Jensen, P. Norby, T. Vegge, Temperature- and pressure-induced changes in the crystal structure of Sr$(NH_3)_8Cl_2$, J. Phys. Chem. C 118 (2014) 24349–24356, https://doi.org/10.1021/jp508076c.
[15] S. Lysgaard, A.L. Ammitzbøll, R.E. Johnsen, P. Norby, U.J. Quaade, T. Vegge, Resolving the stability and structure of strontium chloride amines from equilibrium pressures, XRD and DFT, Int. J. Hydrog. Energy 37 (2012) 18927–18936, https://doi.org/10.1016/j.ijhydene.2012.09.129.
[16] P. Bjerre Jensen, S. Lysgaard, U.J. Quaade, T. Vegge, Designing mixed metal halide ammines for ammonia storage using density functional theory and genetic algorithms, Phys. Chem. Chem. Phys. 16 (2014) 19732–19740, https://doi.org/10.1039/C4CP03133D.
[17] M. Kubota, K. Matsuo, R. Yamanouchi, H. Matsuda, Absorption and desorption characteristics of NH_3 with metal chlorides for ammonia storage, J. Chem. Eng. Jpn. 47 (7) (2014) 542–548, https://doi.org/10.1252/jcej.13we294.
[18] H.S. Jacobsen, H.A. Hansen, J.W. Andreasen, Q. Shi, A. Andreasen, R. Feidenhans'l, M.M. Nielsen, K. Ståhl, T. Vegge, Nanoscale structural characterization of $Mg(NH_3)_6Cl_2$ during NH_3 desorption: an in situ small angle X-ray scattering study, Chem. Phys. Lett. 441 (2007) 255–260, https://doi.org/10.1016/j.cplett.2007.05.001.
[19] L. Jiang, L.W. Wang, Z.Q. Jin, R.Z. Wang, Y.J. Dai, Effective thermal conductivity and permeability of compact compound ammoniated salts in the adsorption/desorption process, Int. J. Therm. Sci. 71 (2013) 103–110, https://doi.org/10.1016/j.ijthermalsci.2013.03.017.
[20] B. Tian, Z.Q. Jin, L.W. Wang, R.Z. Wang, Permeability and thermal conductivity of compact chemical and physical adsorbents with expanded natural graphite as host matrix, Int. J. Heat Mass Transf. 55 (2012) 4453–4459, https://doi.org/10.1016/j.ijheatmasstransfer.2012.04.016.
[21] L.W. Wang, Z. Tamainot-Telto, S.J. Metcalf, R.E. Critoph, R.Z. Wang, Anisotropic thermal conductivity and permeability of compacted expanded natural graphite, Appl. Therm. Eng. 30 (2010) 1805–1811, https://doi.org/10.1016/j.applthermaleng.2010.04.014.
[22] J.H. Han, K.-H. Lee, Gas permeability of expanded graphite–metallic salt composite, Appl. Therm. Eng. 21 (2001) 453–463, https://doi.org/10.1016/S1359-4311(00)00056-9.

[23] M. van der Pal, R.E. Critoph, Performance of $CaCl_2$-reactor for application in ammonia-salt based thermal transformers, Appl. Therm. Eng. 126 (2017) 518–524, https://doi.org/10.1016/j.applthermaleng.2017.07.086.
[24] Y. Yuan, H. Bao, Z. Ma, Y. Lu, A.P. Roskilly, Investigation of equilibrium and dynamic performance of $SrCl_2$-expanded graphite composite in chemisorption refrigeration system, Appl. Therm. Eng. 147 (2019) 52–60, https://doi.org/10.1016/j.applthermaleng.2018.10.071.
[25] S. Wu, T.X. Li, T. Yan, R.Z. Wang, Experimental investigation on a thermochemical sorption refrigeration prototype using EG/$SrCl_2$–NH_3 working pair, Int. J. Refrig. 88 (2018) 8–15, https://doi.org/10.1016/j.ijrefrig.2017.11.030.
[26] S. Wu, T.X. Li, R.Z. Wang, Experimental identification and thermodynamic analysis of ammonia sorption equilibrium characteristics on halide salts, Energy 161 (2018) 955–962, https://doi.org/10.1016/j.energy.2018.07.129.
[27] M. Strobl, I. Manke, N. Kardjilov, A. Hilger, M. Dawson, J. Banhart, Advances in neutron radiography and tomography, J. Phys. D 42 (2009), 243001, https://doi.org/10.1088/0022-3727/42/24/243001.
[28] J. Banhart, A. Borbély, K. Dzieciol, F. Garcia-Moreno, I. Manke, N. Kardjilov, A. R. Kaysser-Pyzalla, M. Strobl, W. Treimer, X-ray and neutron imaging–complementary techniques for materials science and engineering, IJMR 101 (2010) 1069–1079, https://doi.org/10.3139/146.110382.
[29] N. Kardjilov, I. Manke, A. Hilger, M. Strobl, J. Banhart, Neutron imaging in materials science, Mater. Today 14 (2011) 248–256, https://doi.org/10.1016/S1369-7021(11)70139-0.
[30] N. Kardjilov, I. Manke, R. Woracek, A. Hilger, J. Banhart, Advances in neutron imaging, Mater. Today 21 (2018) 652–672, https://doi.org/10.1016/j.mattod.2018.03.001.
[31] Ł. Gondek, N.B. Selvaraj, J. Czub, H. Figiel, D. Chapelle, N. Kardjilov, A. Hilger, I. Manke, Imaging of an operating $LaNi_{4.8}Al_{0.2}$–based hydrogen storage container, Int. J. Hydrog. Energy 36 (2011) 9751–9757, https://doi.org/10.1016/j.ijhydene.2011.05.089.
[32] F. Heubner, A. Hilger, N. Kardjilov, I. Manke, B. Kieback, Ł. Gondek, J. Banhart, L. Röntzsch, In-operando stress measurement and neutron imaging of metal hydride composites for solid-state hydrogen storage, J. Power Sources 397 (2018) 262–270, https://doi.org/10.1016/j.jpowsour.2018.06.093.
[33] P. Boillat, E.H. Lehmann, P. Trtik, M. Cochet, Neutron imaging of fuel cells–recent trends and future prospects, Curr. Opin. Electrochem. 5 (2017) 3–10, https://doi.org/10.1016/j.coelec.2017.07.012.
[34] A. Senyshyn, M.J. Mühlbauer, K. Nikolowski, T. Pirling, H. Ehrenberg, In-operando" neutron scattering studies on Li-ion batteries, J. Power Sources 203 (2012) 126–129, https://doi.org/10.1016/j.jpowsour.2011.12.007.
[35] W.J. Weydanz, H. Reisenweber, A. Gottschalk, M. Schulz, T. Knoche, G. Reinhart, M. Masuch, J. Franke, R. Gilles, Visualization of electrolyte filling process and influence of vacuum during filling for hard case prismatic lithium ion cells by neutron imaging to optimize the production process, J. Power Sources 380 (2018) 126–134, https://doi.org/10.1016/j.jpowsour.2018.01.081.
[36] C. Tötzke, I. Manke, A. Hilger, G. Choinka, N. Kardjilov, T. Arlt, H. Markötter, A. Schröder, K. Wippermann, D. Stolten, C. Hartnig, P. Krüger, R. Kuhn, J. Banhart, Large area high resolution neutron imaging detector for fuel cell research, J. Power Sources 196 (2011) 4631–4637, https://doi.org/10.1016/j.jpowsour.2011.01.049.
[37] P. Berdiyeva, A. Karabanova, M.G. Makowska, R.E. Johnsen, D. Blanchard, B. C. Hauback, S. Deledda, In-situ neutron imaging study of NH_3 absorption and desorption in $SrCl_2$ within a heat storage prototype reactor, J. Energy Storage 29 (2020), 101388, https://doi.org/10.1016/j.est.2020.101388.
[38] S.N. Gunasekara, S. Soprani, A. Karabanova, V. Martin, D. Blanchard, Numerical design of a reactor-heat exchanger combined unit for ammonia-$SrCl_2$ thermochemical storage system, in: ISES SWC2019, 2019, pp. 1–12, in: http://proceedings.ises.org/?conference=*&mode=page.
[39] Y. Wang, C.H. Peden, S. Choi, Catalyst of a metal heteropoly acid salt that is insoluble in a polar solvent on a non-metallic porous support and method of making, in: US6815392B2, Washington, DC: U.S. Patent and Trademark Office, 2004. https://patents.google.com/patent/US6815392B2/en. accessed April 26, 2020.
[40] C. Tötzke, N. Kardjilov, N. Lenoir, N. Lenoir, I. Manke, S.E. Oswald, A. Tengattini, A. Tengattini, What comes NeXT? – high-speed neutron tomography at ILL, Optics Express 27 (2019) 28640–28648, https://doi.org/10.1364/OE.27.028640. OE.
[41] C.A. Schneider, W.S. Rasband, K.W. Eliceiri, NIH Image to ImageJ: 25 years of image analysis, Nat. Methods 9 (2012) 671–675, https://doi.org/10.1038/nmeth.2089.
[42] Radioscopy & Tomography systems | RX Solutions, Rx-Solutions. https://www.rxsolutions.fr/x-act (accessed May 11, 2020).
[43] VGSTUDIO MAX: High-End Software for CT Data, volumegraphics.com. https://www.volumegraphics.com/en/products/vgstudio-max.html (accessed May 11, 2020).